EGRET Diffuse Gamma Ray Maps Between 30 MeV and 10 GeV

A. N. Cillis[1], R. C. Hartman

Code 661, NASA's Goddard Space Flight Center, Greenbelt, MD 20771

ABSTRACT

This paper presents all-sky maps of diffuse gamma radiation in various energy ranges between 30 MeV and 10 GeV, based on data collected by the EGRET instrument on the Compton Gamma Ray Observatory. Although the maps can be used for a variety of applications, the immediate goal is the generation of diffuse gamma-ray maps which can be used as a diffuse background/foreground for point source analysis of the data to be obtained from new high-energy gamma-ray missions like GLAST and AGILE. To generate the diffuse gamma maps from the raw EGRET maps, the point sources in the Third EGRET Catalog were subtracted out using the appropriate point spread function for each energy range. After that, smoothing was performed to minimize the effects of photon statistical noise. A smoothing length of 1° was used for the Galactic plane maps. For the all-sky maps, a procedure was used which resulted in a smoothing length roughly equivalent to 4°. The result of this work is 16 maps of different energy intervals for $|b| \leq 20°$, and 32 all-sky maps, 16 in equatorial coordinates (J2000) and 16 in Galactic coordinates.

Subject headings: cosmic rays — diffuse radiation — gamma rays: observations

1. Introduction

In the last four decades several experiments have explored the sky searching for high-energy gamma-ray emission. The dominant feature found was a band of diffuse emission along the Galactic Plane. In addition to this Galactic feature, whose origin is reasonably well understood, the diffuse gamma radiation contains a second component that appears to be at least roughly isotropic. Its origin is not established, although a wide variety of suggestions have been put forward.

---

[1]NRC Resident Research Associate

The Galactic component is strongest within $\pm 60°$ of the Galactic Center in longitude and $\pm 10°$ of the Galactic Plane in latitude, where the most interstellar gas is present, and falls off rapidly at higher latitudes. It was first detected with an instrument on OSO-3 (Kraushaar et al. 1972) and with a high altitude balloon experiment (Kniffen & Fichtel 1970; Fichtel et al. 1972). These observations were followed by Galactic plane surveys by SAS-2 (Kniffen et al. 1973; Fichtel et al. 1975; Hartman et al. 1979) and by COS-B (Mayer-Hasselwander et al. 1982). More recently, the EGRET instrument on the Compton Gamma Ray Observatory provided more than an order of magnitude increase in sensitivity over previous experiments, as well as low instrumental background, and thus provided a much more detailed look at the Galactic gamma radiation (Bertsch et al. 1993; Hunter et al. 1997).

There is general agreement that the Galactic diffuse gamma radiation comes primarily from the interaction of cosmic rays with the interstellar matter and interstellar photons (Kniffen et al. 1973; Fichtel et al. 1975; Bignami et al. 1975; Bertsch et al. 1993; Hunter et al. 1997; Strong et al. 2004a; Strong et al. 2004b; Strong et al. 2004c). The principal processes that produce this gamma radiation are neutral pion production by cosmic-ray nucleons interacting with nucleons in the interstellar gas (followed by decay of the pions to gammas), bremsstrahlung by cosmic-ray electrons, and inverse Compton scattering of cosmic-ray electrons by soft interstellar photons.

SAS-2 also indicated for the first time the presence of "isotropic" gamma emission, presumably of extragalactic origin (Fichtel et al. 1975; Fichtel et al. 1977; Thompson & Fichtel 1982). Sreekumar et al. (1998) carried out a similar high latitude study with EGRET data, arriving at a compatible intensity with greatly reduced error bars. This could in principal be truly diffuse radiation, but has also been explained as a superposition of unresolved point sources. Unresolved blazars is the most popular class (Bignami et al. 1979; Padovani et al. 1993; Stecker & Salamon 1996; Mukherjee & Chiang 1999; Mücke & Pohl 2000), but contributions from other active galaxies (Kazanas & Protheroe 1983) as well as normal galaxies (Setti & Woltjer 2000; Pavlidou & Fields 2002) have been investigated also.

Diffuse mechanisms suggested include scenarios with baryon-antibaryon symmetry (Stecker 2002 and references therein), primordial black hole evaporation (Page & Hawking 1976), and annihilation of supersymmetric particles (Silk & Srednickin 1984; Rudaz & Stecker 1991). All these theories predict continuum or line contributions that are unobservable above 30 MeV with the instruments available up to now. Recent work (Loeb and Waxman 2000; Keshet et al. 2003) attributes the isotropic gamma radiation to shocks induced by gravity during the formation of large-scale structure in the intergalactic medium, in the end producing a population of highly-relativistic electrons. These electrons scatter a small fraction of the microwave background photons in the present day universe up to gamma-ray energies,

thereby providing the gamma-ray background. The predicted diffuse intensity agrees with the observed background over more than four decades in photon energy, and implies a mean cosmological density of baryons which is consistent with Big Bang nucleosynthesis.

There are two major motivations for the work presented here: First, for the gamma ray missions that will be deployed in the next several years, AGILE (2005) and GLAST (2007), it is necessary to have maps of the diffuse gamma ray emission in order to be able to search for and identify point sources. For EGRET, this function was initially carried out using a theoretical model of the Galactic emission; eventually this model was "tuned" to agree (at least roughly) with the diffuse gamma radiation detected by EGRET. However, in that diffuse model, the energy spectrum of the Galactic emission was assumed to be the same everywhere; in this paper, the maps for different energy ranges are independent. The second motivation is to provide source-subtracted gamma-ray maps for a wide range of energy bands, enabling a variety of theoretical studies on the diffuse radiation.

In this work we present all-sky maps of diffuse gamma radiation (point source subtracted) in 16 energy ranges between 30 MeV and 10 GeV, in both Galactic and equatorial coordinates. For the same 16 energy ranges, maps are provided of the Galactic Plane region ($|b| \leq 20°$), with better angular resolution. Similar maps, based on less data and less complete point source subtraction, have been published in the past (Hunter et al. 1997), but for very limited energy selection.

Section 2 describes briefly the EGRET instrument and the data used. This is followed in Section 3 with a description of the procedure used to generate these maps. The maps are shown in Section 4; the complete set of maps is available electronically, in both eps and FITS formats. The last (Discussion) section includes notes on various limitations and cautions regarding the use of these maps.

2. The EGRET Data

EGRET detected gamma rays in the energy range from 30 MeV to over 30 GeV, with an energy resolution of 20%-25% over most of that range. The instrument is described in Hughes et al. (1980), Kanbach (1988, 1989), Thompson et. al (1993) and Esposito et al. (1998). The work described here started with standard EGRET all-sky maps (ftp://cossc.gsfc.nasa.gov/compton/data/egret/high_level/combined_data) of photon counts, instrument exposure, and gamma-ray intensity, binned in 0.5° pixels, in both Galactic and equatorial coordinates. The energy ranges in MeV are: (narrow ranges) 30-50, 50-70, 70-100, 100-150, 150-300, 300-500, 500-1000, 1000-2000, 2000-4000, 4000-10000; (broader

ranges) 30-100, 100-300, 300-1000; (integral ranges) >100, >300, >1000.

3. Procedure used to generate the maps

The point source subtraction used the sources in the Third EGRET Catalog (3EG) (Hartman et al. 1999) that showed significant >100 MeV emission when averaged over the entire time interval of the maps (1991 April to 1995 October, cycles 1, 2, 3 and 4 of the mission), plus excesses below the catalog threshold ($\geq 5\sigma$ within 10° of the Galactic plane, $\geq 4\sigma$ elsewhere), down to 3σ. The below-threshold excesses account for an average sky intensity of about 10^{-6} cm^{-2} s^{-1} sr^{-1}, an order of magnitude below the extragalactic diffuse intensity. Because of their higher concentration near the Galactic plane, the average effect of their removal is even lower than 10%. The more important effect is the elimination of "bumps" whose size is consistent with the psf. Simulations have indicated that 10-20% of the below-threshold excesses are likely to be statistical noise; after the smoothing described below, their removal has a negligible effect on the overall character of the final maps.

It is important to note that, in the point source subtraction, no spectral indices were assumed for the sources or the below-3EG-threshold excesses. In each energy range, the flux from each source (or excess) was determined using the EGRET likelihood program.

Using standard EGRET software, maps were created for each energy range, and for both Galactic and equatorial coordinates, containing only the point spread functions for the sources to be subtracted, with fluxes as determined by the standard EGRET likelihood software. Each of those maps was then multiplied by the exposure map for the appropriate energy range, after which the product maps were subtracted from the standard all-sky maps. Figure 1 shows the point spread functions for each of the ten narrow energy ranges, the three broader ranges, and the three integral ranges. The psf for each energy range is an energy-weighted average, for an assumed photon spectral index of 2.1. Within the 30° aspect angle chosen for the standard maps, the EGRET psf had no significant dependence on instrument aspect angle.

Effects of photon statistical noise were minimized by performing Gaussian smoothing. Because they contain higher photon intensities, maps of the Galactic plane region ($|b| \leq 20°$) were created with a smoothing length of 1°. For the all-sky maps, a more complicated procedure was necessary, which resulted in a smoothing length roughly equivalent to 4°. Despite this smoothing, some of the maps at the highest and lowest energies (where the effective area and/or intensity is least) show considerable photon statistical noise, as illustrated later.

In addition to the reduction in photon statistical noise, the smoothing reduces or e-

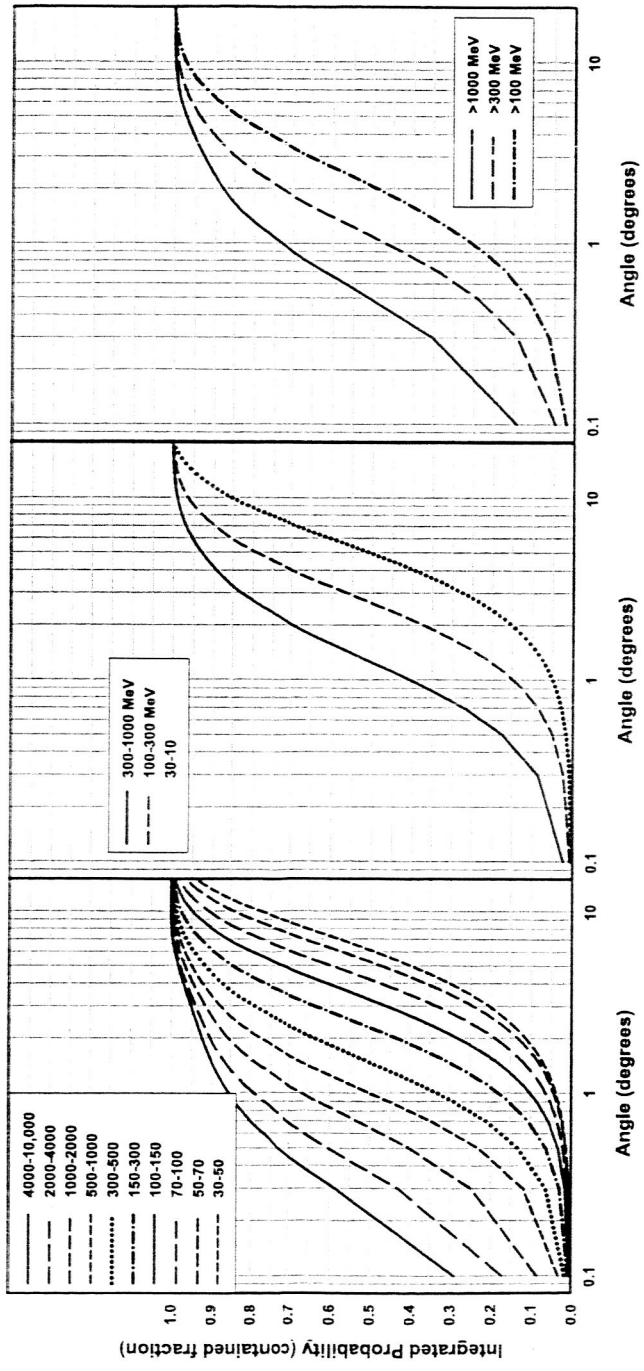

Fig. 1.— EGRET PSF function: Integrated probability versus angle.

liminates two types of artifacts that are seen in the unsmoothed maps: 1) effects of psf imperfections where strong sources have been subtracted (Around weaker sources, statistical noise dominates over the imperfections.); 2) field-of-view edge effects, probably caused by small errors in the shape of the sensitivity calibration as a function of aspect angle. The latter type of artifact shows up as 30° arcs separating regions of slightly different intensities. (30° is the radius of the field of view used in generating the original all-sky maps.)

The raw EGRET all-sky maps are rectangular, but they extend all the way to 90°. Because of the extreme distortions, there are defects in the intensities in many of the high latitude pixels. These were "repaired" by comparing the Galactic and the equatorial maps. In the final maps, pixels adjacent to a pole in a Galactic (or equatorial) map assume the intensity of the same sky position in the corresponding equatorial (or Galactic) map. At slightly greater separations from a pole, weighted intensities were used, with weights determined by angular distance from the respective poles.

4. Results

We have generated maps for 16 different energy intervals. The Galactic plane maps ($|b| \leq 20°$) are smoothed at 1°. The 16 equatorial coordinate (J2000) and 16 Galactic coordinate maps are smoothed at roughly 4°. The energy intervals (in MeV) of the maps are the followings: Ten narrow ranges, (30-50, 50-70, 70-100, 100-150, 150-300, 300-500, 500-1000, 1000-2000, 2000-4000, 4000-10000), three broader ranges (30-100, 100-300, 300-1000), and three integral ranges (E>100, E>300, E>1000). The numbers of photons above 10,000 MeV is small compared with the number between 1000 and 10,000 MeV, so E>1000 MeV is effectively 1000-10,000 MeV. Despite the smoothing that has been done, all of the maps are subject to some statistical uncertainty; the broader energy ranges and integral range maps are useful to obtain improved statistics if the narrow energy ranges are not required.

Figure 2(a-p) contains the sixteen Galactic plane maps. Figures 2(a) and 2(j), narrow energy-range maps for the highest and lowest EGRET energy ranges, are the maps with the poorest photon statistics. Especially in the less intense portions, the statistical fluctuations are obvious. Note that for 30-50 MeV, the point spread function is several times larger than the 1° smoothing length used, while the opposite is true for 4000-10,000 MeV. The broad energy-range 100-300 MeV, Figure 2(l), and the integral range >100 MeV, Figure 2(n), have the best photon statistics of all the Galactic plane maps. They show little or no evidence for photon noise, because the 100-300 MeV energy range is where the product of EGRET effective area and diffuse gamma-ray intensity is maximized.

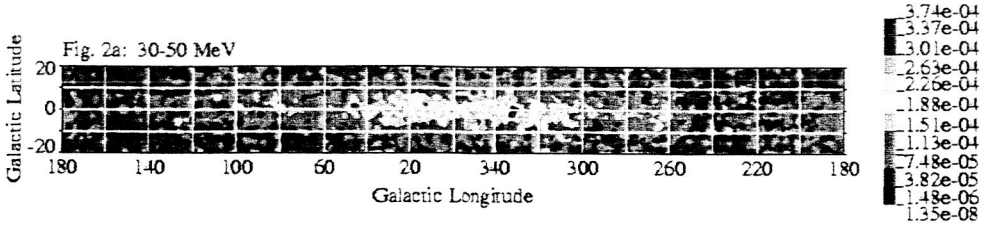
Fig. 2a: 30-50 MeV
Galactic Latitude
20
0
-20
180 140 100 60 20 340 300 260 220 180
Galactic Longitude
3.74e-04
3.37e-04
3.01e-04
2.63e-04
2.26e-04
1.88e-04
1.51e-04
1.13e-04
7.48e-05
3.82e-05
1.48e-06
1.35e-08

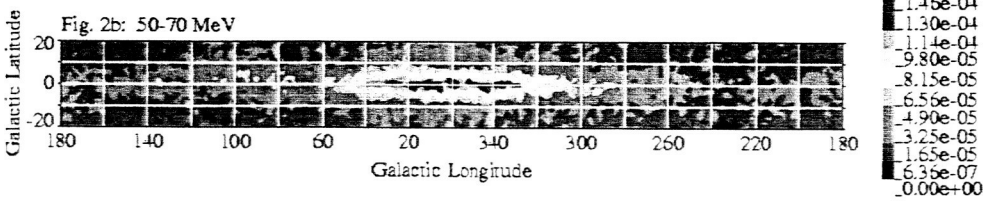
Fig. 2b: 50-70 MeV
Galactic Latitude
20
0
-20
180 140 100 60 20 340 300 260 220 180
Galactic Longitude
1.62e-04
1.46e-04
1.30e-04
1.14e-04
9.80e-05
8.15e-05
6.56e-05
4.90e-05
3.25e-05
1.65e-05
6.35e-07
0.00e+00

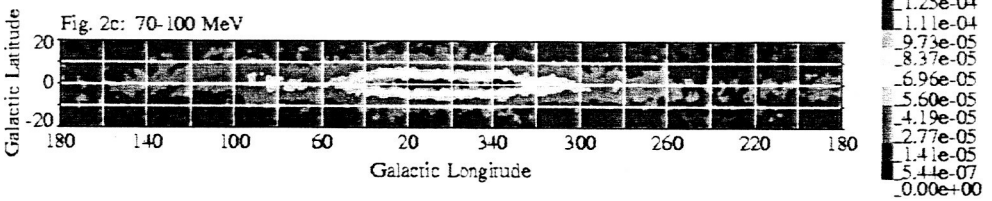
Fig. 2c: 70-100 MeV
Galactic Latitude
20
0
-20
180 140 100 60 20 340 300 260 220 180
Galactic Longitude
1.39e-04
1.25e-04
1.11e-04
9.73e-05
8.37e-05
6.96e-05
5.60e-05
4.19e-05
2.77e-05
1.41e-05
5.44e-07
0.00e+00

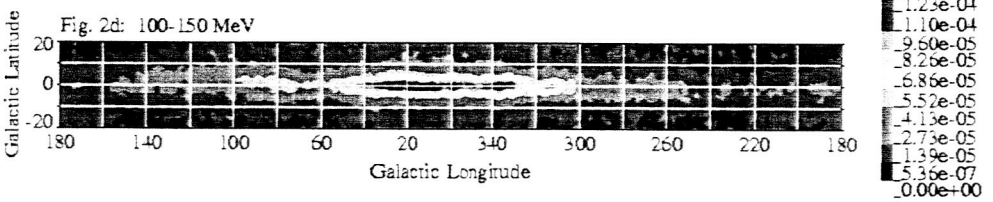
Fig. 2d: 100-150 MeV
Galactic Latitude
20
0
-20
180 140 100 60 20 340 300 260 220 180
Galactic Longitude
1.37e-04
1.23e-04
1.10e-04
9.60e-05
8.26e-05
6.86e-05
5.52e-05
4.13e-05
2.73e-05
1.39e-05
5.36e-07
0.00e+00

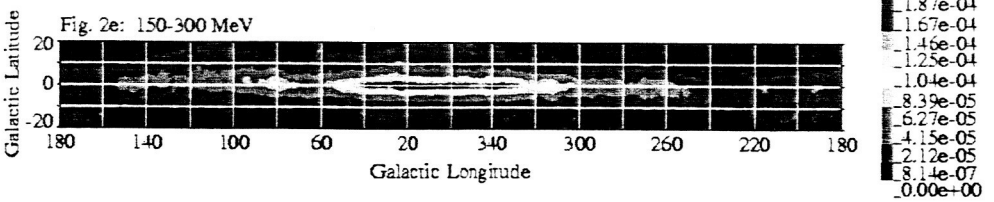
Fig. 2e: 150-300 MeV
Galactic Latitude
20
0
-20
180 140 100 60 20 340 300 260 220 180
Galactic Longitude
2.08e-04
1.87e-04
1.67e-04
1.46e-04
1.25e-04
1.04e-04
8.39e-05
6.27e-05
4.15e-05
2.12e-05
8.14e-07
0.00e+00

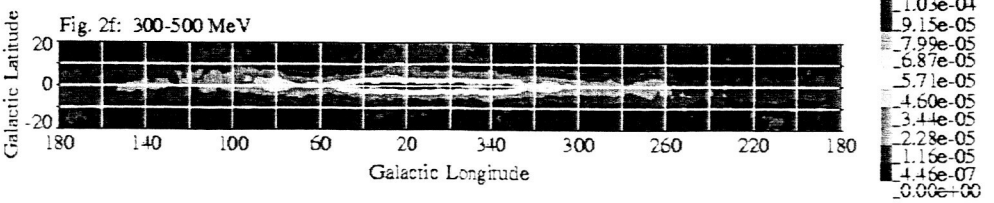
Fig. 2f: 300-500 MeV
Galactic Latitude
20
0
-20
180 140 100 60 20 340 300 260 220 180
Galactic Longitude
1.14e-04
1.03e-04
9.15e-05
7.99e-05
6.87e-05
5.71e-05
4.60e-05
3.44e-05
2.28e-05
1.16e-05
4.46e-07
0.00e+00

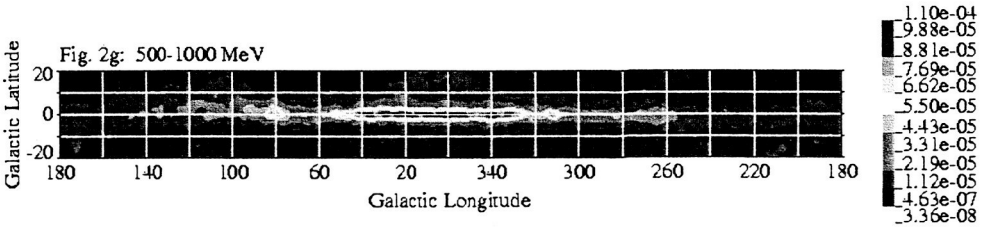
Fig. 2g: 500-1000 MeV
Galactic Latitude
20
0
-20
180 140 100 60 20 340 300 260 220 180
Galactic Longitude
1.10e-04
9.88e-05
8.81e-05
7.69e-05
6.62e-05
5.50e-05
4.43e-05
3.31e-05
2.19e-05
1.12e-05
4.63e-07
3.36e-08

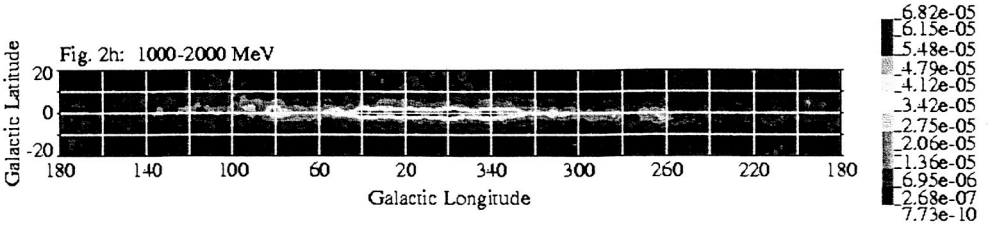
Fig. 2h: 1000-2000 MeV
Galactic Latitude
20
0
-20
180 140 100 60 20 340 300 260 220 180
Galactic Longitude
6.82e-05
6.15e-05
5.48e-05
4.79e-05
4.12e-05
3.42e-05
2.75e-05
2.06e-05
1.36e-05
6.95e-06
2.68e-07
7.73e-10

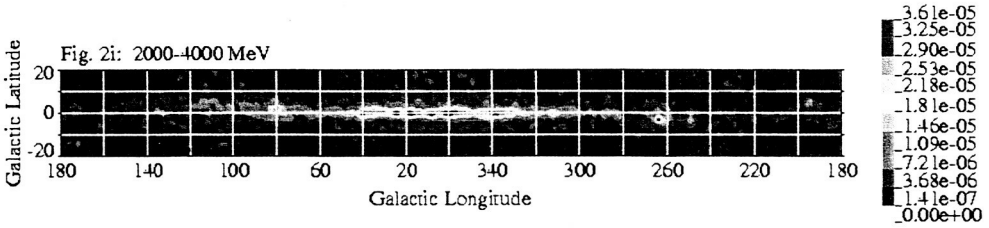
Fig. 2i: 2000-4000 MeV
Galactic Latitude
20
0
-20
180 140 100 60 20 340 300 260 220 180
Galactic Longitude
3.61e-05
3.25e-05
2.90e-05
2.53e-05
2.18e-05
1.81e-05
1.46e-05
1.09e-05
7.21e-06
3.68e-06
1.41e-07
0.00e+00

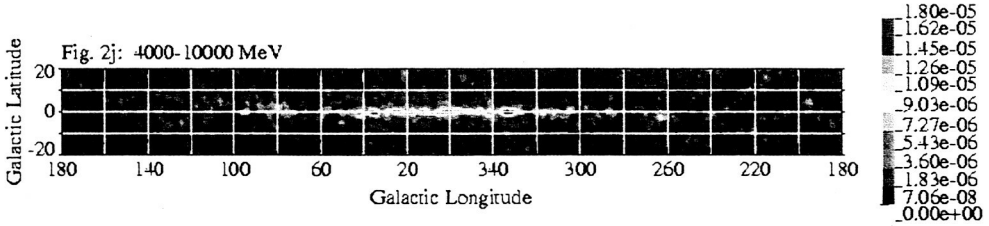
Fig. 2j: 4000-10000 MeV
Galactic Latitude
20
0
-20
180 140 100 60 20 340 300 260 220 180
Galactic Longitude
1.80e-05
1.62e-05
1.45e-05
1.26e-05
1.09e-05
9.03e-06
7.27e-06
5.43e-06
3.60e-06
1.83e-06
7.06e-08
0.00e+00

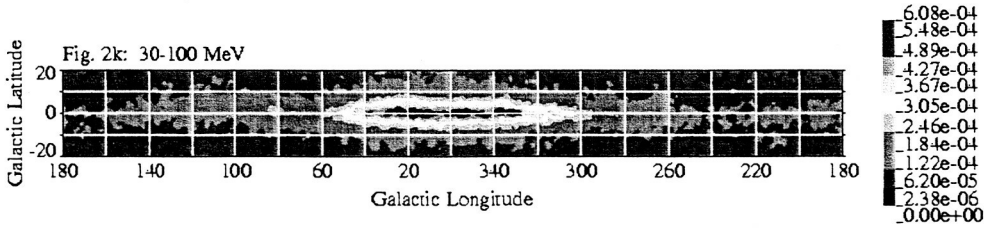
Fig. 2k: 30-100 MeV
Galactic Latitude
20
0
-20
180 140 100 60 20 340 300 260 220 180
Galactic Longitude
6.08e-04
5.48e-04
4.89e-04
4.27e-04
3.67e-04
3.05e-04
2.46e-04
1.84e-04
1.22e-04
6.20e-05
2.38e-06
0.00e+00

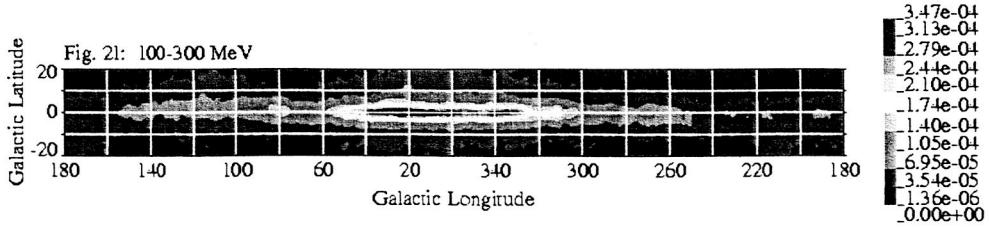
Fig. 2l: 100-300 MeV
Galactic Latitude
20
0
-20
180 140 100 60 20 340 300 260 220 180
Galactic Longitude
3.47e-04
3.13e-04
2.79e-04
2.44e-04
2.10e-04
1.74e-04
1.40e-04
1.05e-04
6.95e-05
3.54e-05
1.36e-06
0.00e+00

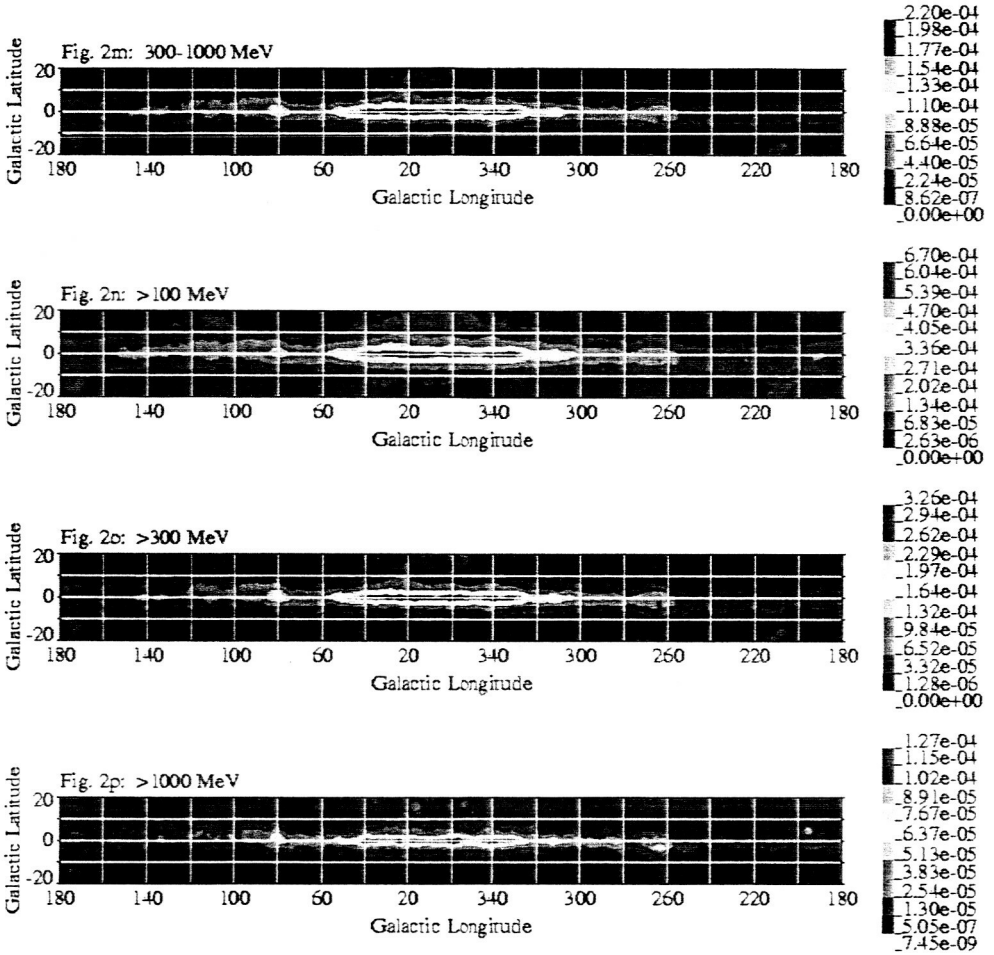

Fig. 2.— Galactic plane maps: (a) 30-50 MeV, (b) 50-70 MeV, (c) 70-100 MeV, (d) 100-150 MeV, (e) 150-300 MeV, (f) 300-500 MeV, (g) 500-1000 MeV, (h) 1000-2000 MeV, (i) 2000-4000 MeV, (j) 4000-10,000 MeV, (k) 30-100 MeV, (l) 100-300 MeV, (m) 300-1000 MeV, (n) >100 MeV, (o) >300 MeV, (p) >1000 MeV. Units of intensity are photons cm^{-2} sr^{-1} s^{-1}. Smoothing length is 1°. Figures 2(a-p) are available in the electronic edition of the Journal. The printed edition contains only a sample, 2(a), 2(j), and 2(l).

The all-sky Galactic and equatorial projection maps are in Figures 3(a-p) and 4(a-p), respectively.

By comparing common regions in Figures 2 and 3, the effect of the two different smoothing lengths is apparent.

With the FITS format maps, available at gamma.gsfc.nasa.gov via anonymous ftp, contour intervals can be adjusted (or ignored) as desired, or further smoothing can be applied if needed.

5. Discussion

Several precautions must be observed in using the maps presented here: First, although the extreme cases of weaker photon statistics are shown in Figures 2(a) and 2(j), other maps may contain significant photon noise. In general, if a feature is not observed in several adjacent energy ranges, it must be regarded with strong skepticism. If appropriate, additional smoothing can be done on the FITS version of a map. If the (new) smoothing length is less than $\sim 1/3$ the size of the psf for that energy range (see Figure 1), the angular resolution of the map will not be significantly degraded.

Next, as mentioned by Hartman et al. (1999), the very bright point source 3EG 0834-4511 (Vela pulsar) causes artifacts in the region within a few degrees. This arises from two effects: inaccuracies in the point spread function, and statistical fluctuations of the (large) counts in the pixels around the pulsar position. Similar but smaller effects are seen in unsmoothed maps around other bright sources. The smoothing done in this work reduces the magnitude of those artifacts, but in the Galactic plane maps, there are still very noticeable effects around the Vela pulsar. Thus it would be inadvisable to draw conclusions concerning diffuse intensities within 5° of that object. The smoothing seems to avoid similar artifacts around other bright sources such as 3EG J0633+1751 = Geminga Pulsar, 3EG J0534+2200 = PSR B0534+21 = Crab Pulsar, and the extragalactic source 3EG J1255-0549 = 3C 279.

It is interesting to compare the minimum intensity in the various all-sky maps with the intensities given for the same energy ranges in the Sreekumar at al. (1998) study of the "isotropic" intensity. In the middle energy ranges, between 70 and 500 MeV, the map minima are very similar to the values in Sreekumar et al. (1998). However, at higher and lower energies, the minima in the maps presented here are lower than the values in Sreekumar et al., by 50-70% in the 30-50 MeV range, and by 85-95% at 4000-10,000 MeV. Although statistical fluctuations may account for the large discrepancy in the later case, the reason for the lower energy effect is unclear. It must be recalled that, although Sreekumar et al. (1998)

Fig. 3a: 30-50 MeV

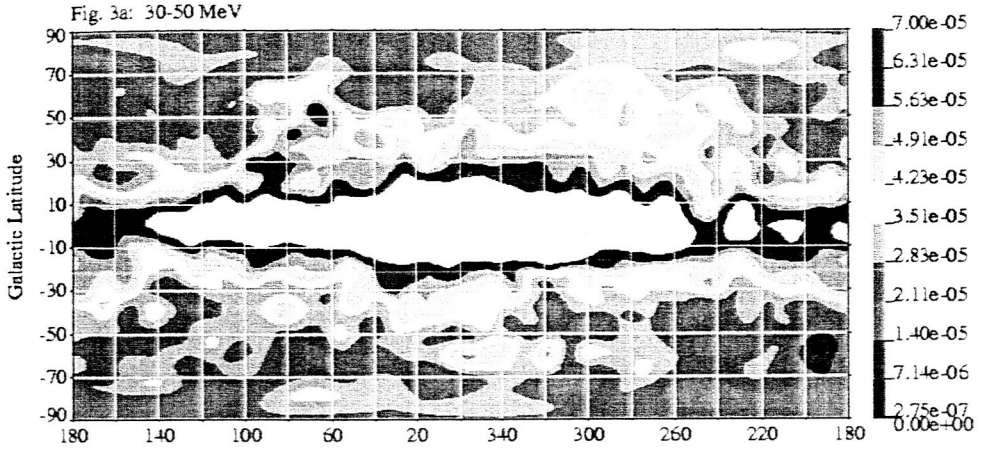

Fig. 3b: 50-70 MeV

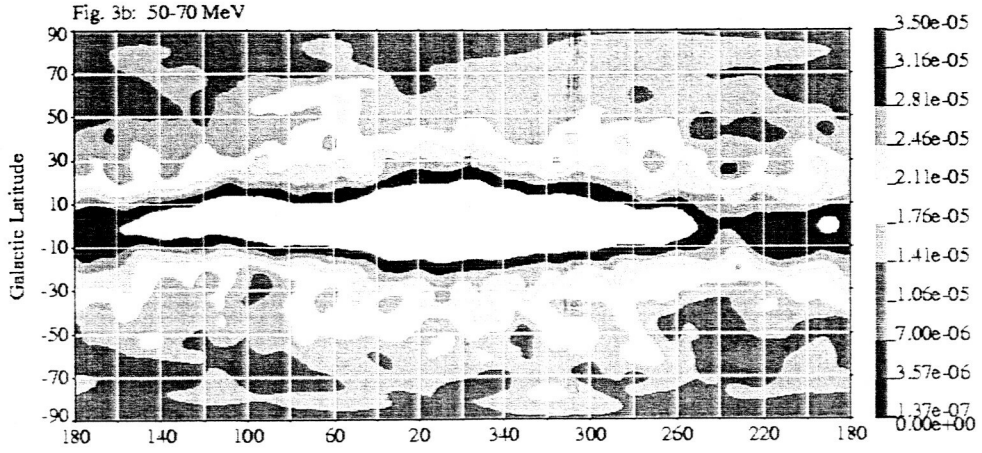

Fig. 3c: 70-100 MeV

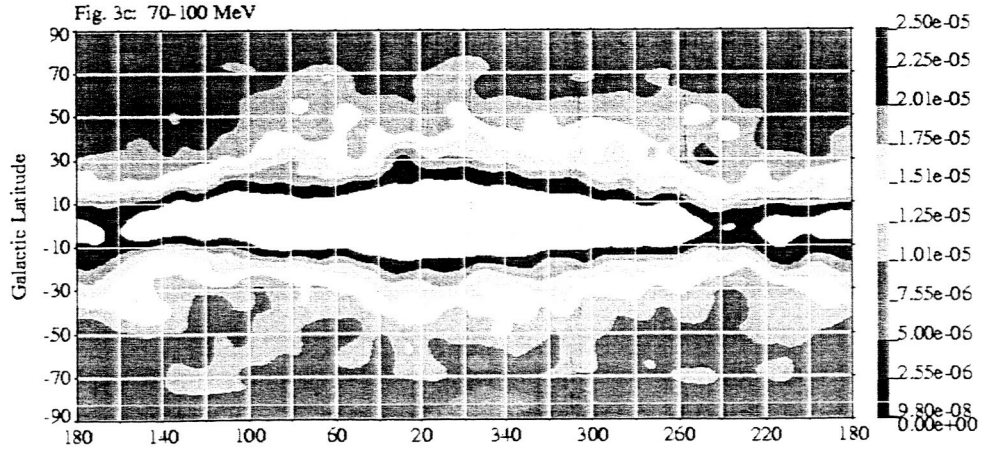

Fig. 3d: 100-150 MeV

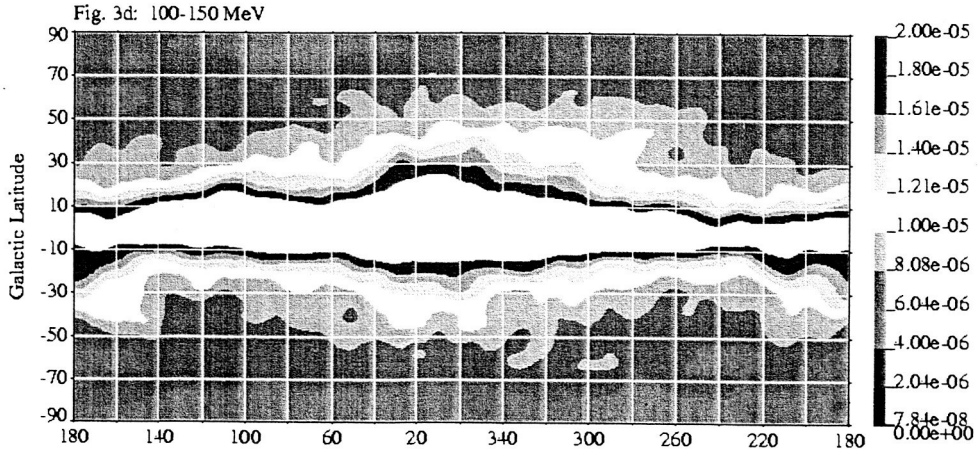

Fig. 3e: 150-300 MeV

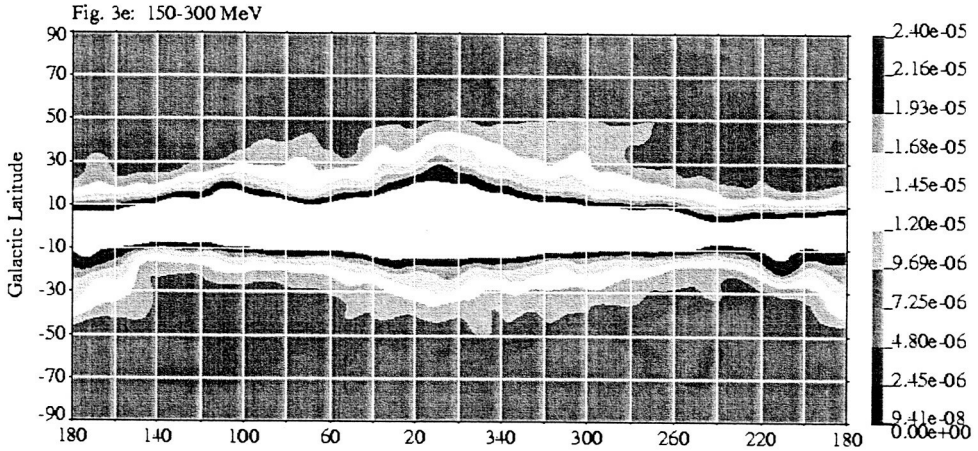

Fig. 3f: 300-500 MeV

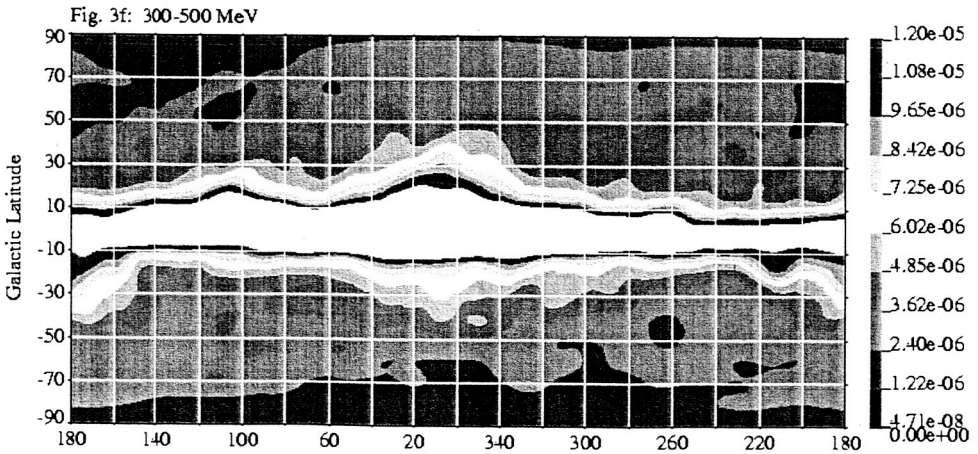

Fig. 3g: 500-1000 MeV

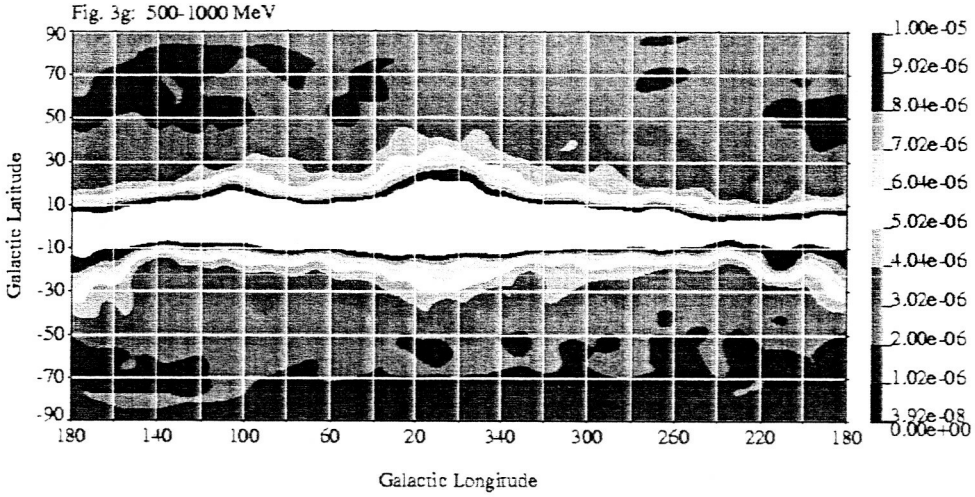

Fig. 3h: 1000-2000 MeV

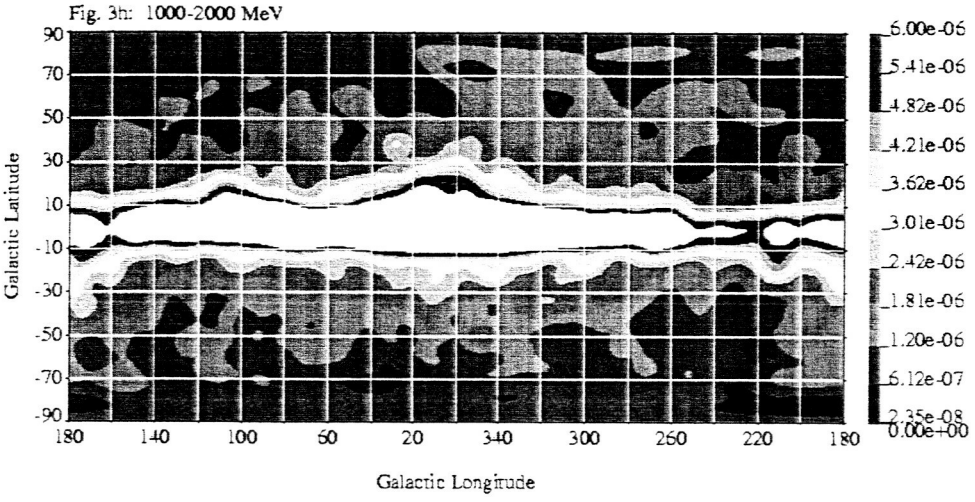

Fig. 3i: 2000-4000 MeV

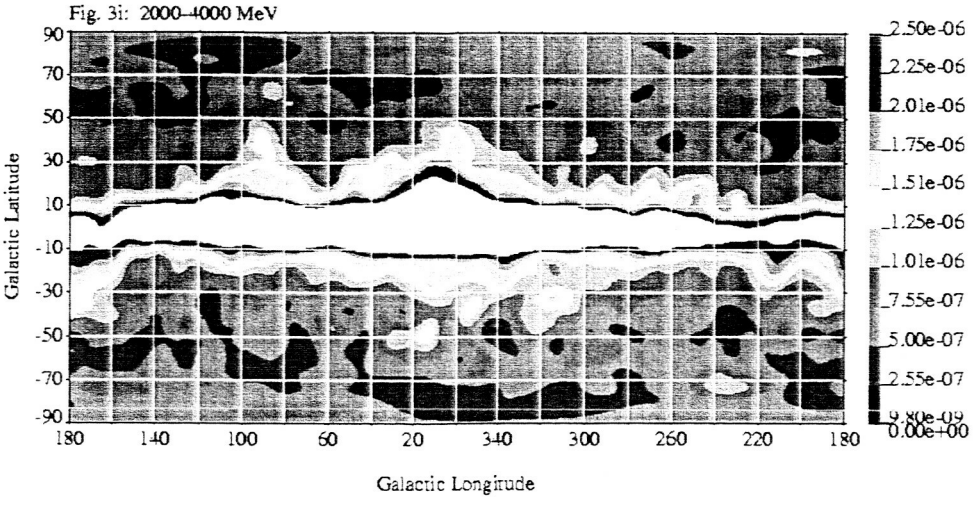

Fig. 3j: 4000-10000 MeV

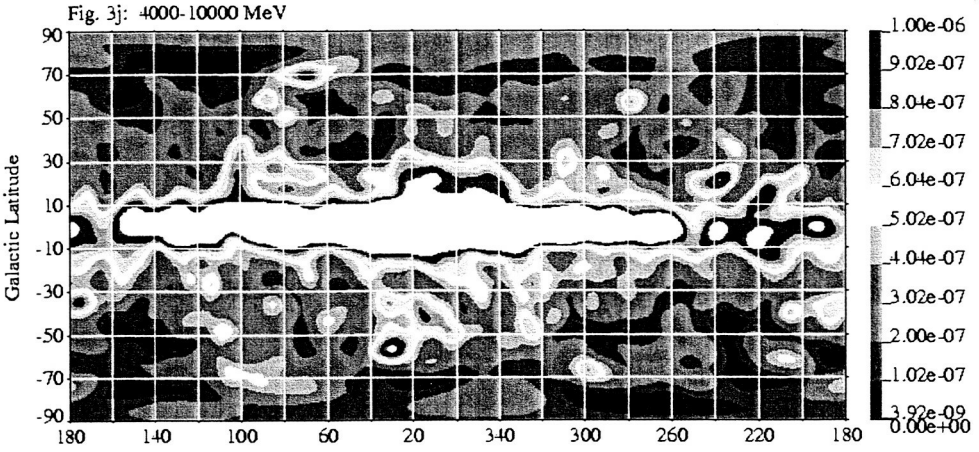

Fig. 3k: 30-100 MeV

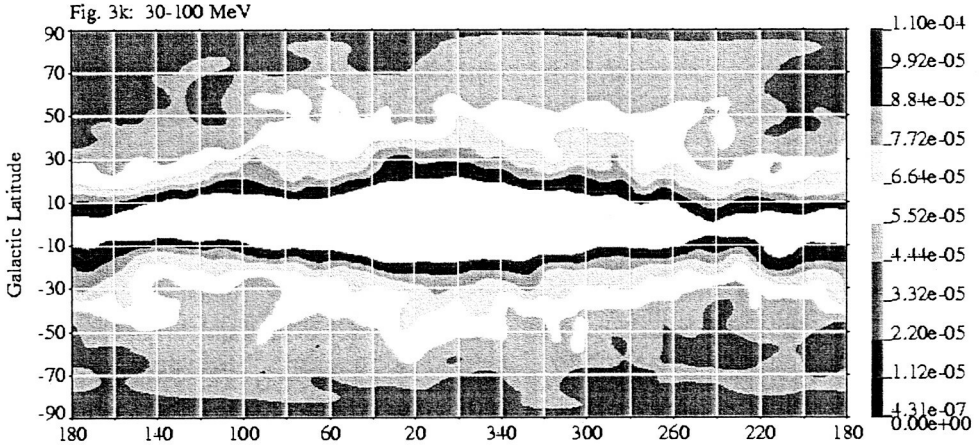

Fig. 3l: 100-300 MeV

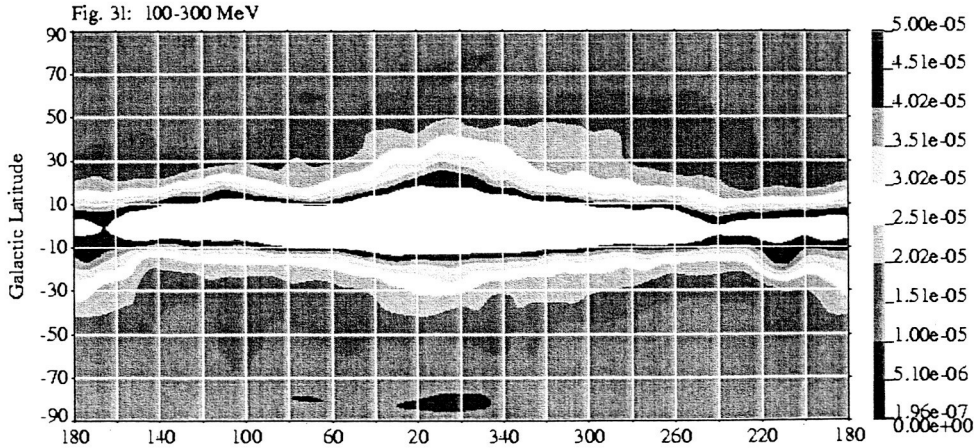

Fig. 3m: 300-1000 MeV

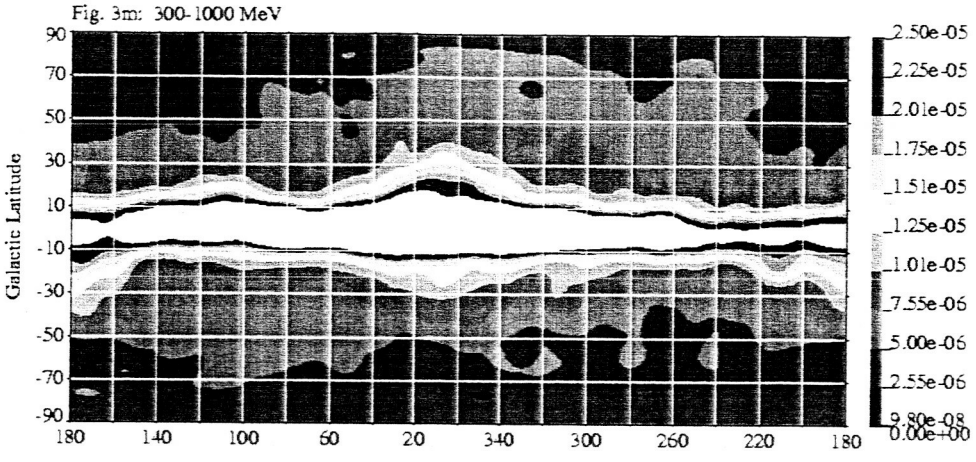

Fig. 3n: >100 MeV

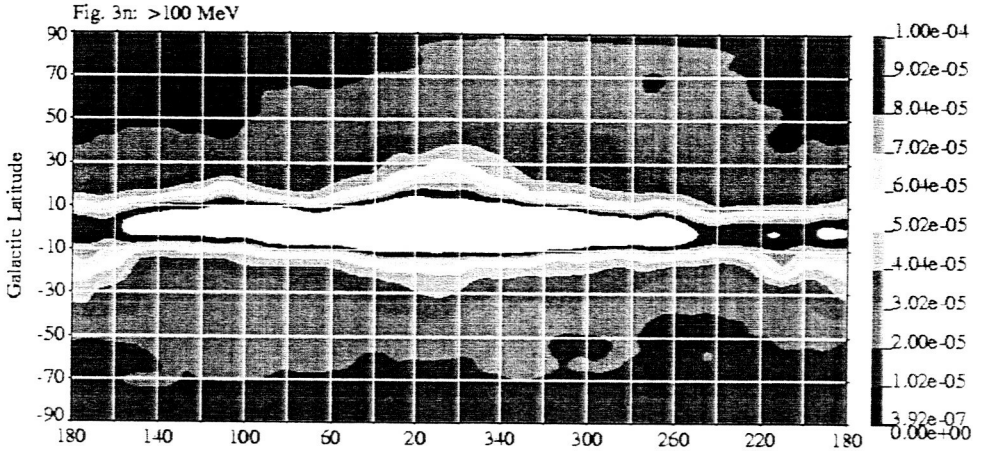

Fig. 3o: >300 MeV

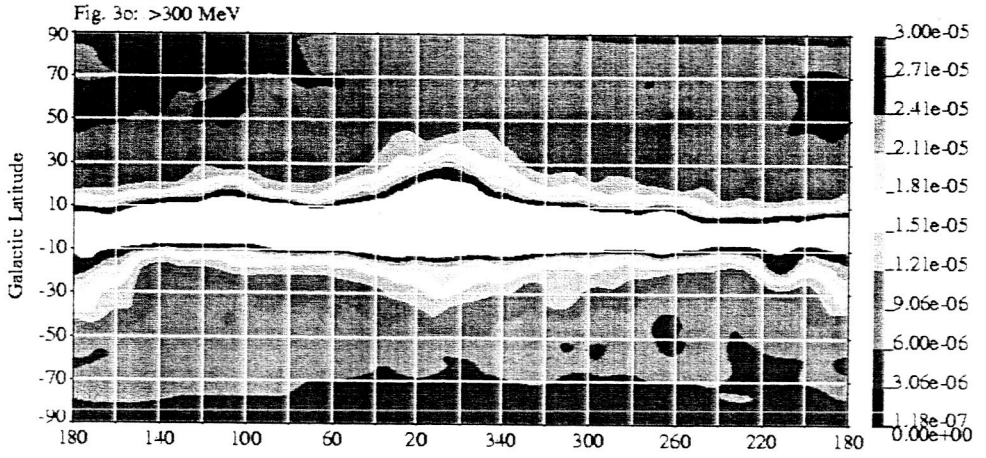

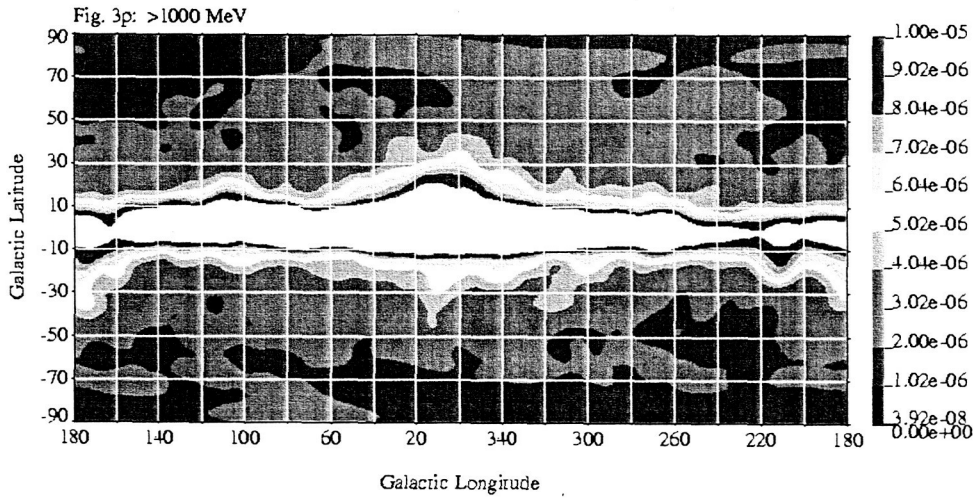

Fig. 3.— All-sky Galactic projection maps: (a) 30-50 MeV, (b) 50-70 MeV, (c) 70-100 MeV, (d) 100-150 MeV, (e) 150-300 MeV, (f) 300-500 MeV, (g) 500-1000 MeV, (h) 1000-2000 MeV, (i) 2000-4000 MeV, (j) 4000-10,000 MeV, (k) 30-100 MeV, (l) 100-300 MeV, (m) 300-1000 MeV, (n) >100 MeV, (o) >300 MeV, (p) >1000 MeV. Units of intensity are photons cm^{-2} sr^{-1} s^{-1}. Smoothing length is roughly 4°. Figures 3(a-p) are available in the electronic edition of the Journal. The printed edition contains only a sample, 3(l).

Fig. 4a: 30-50 MeV

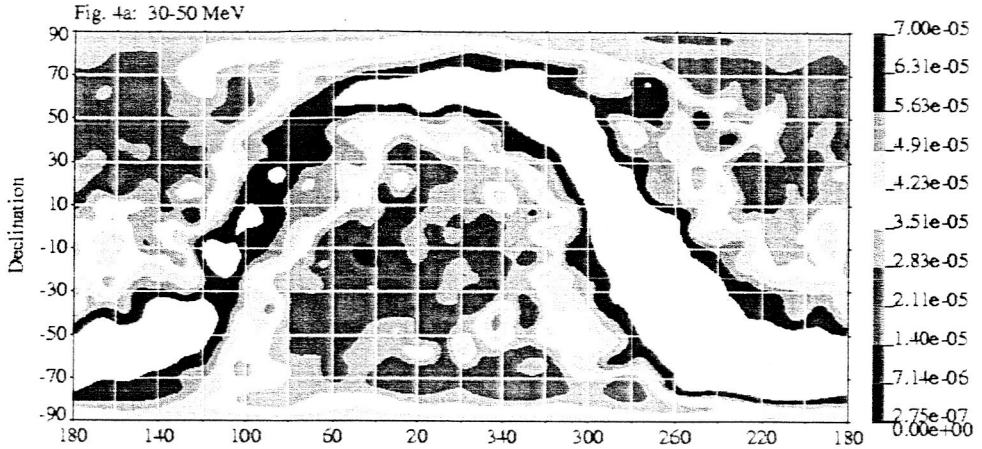

Fig. 4b: 50-70 MeV

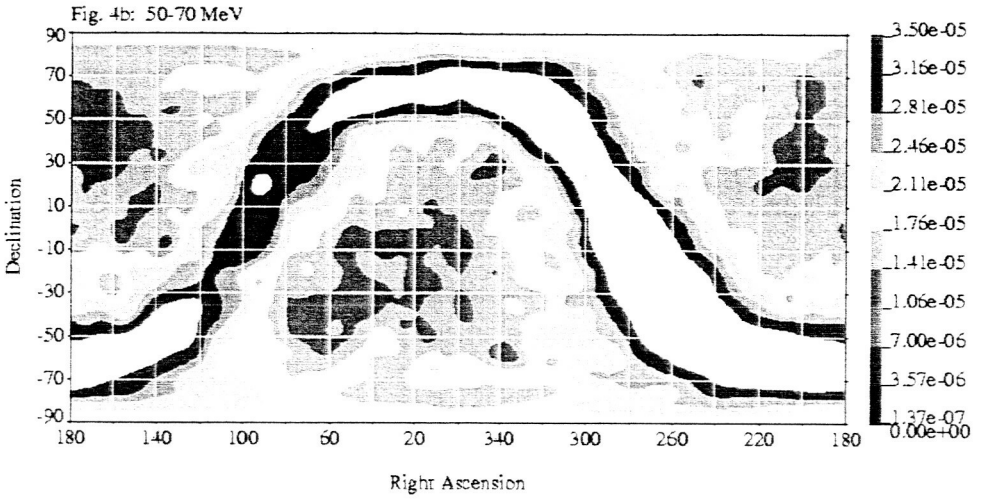

Fig. 4c: 70-100 MeV

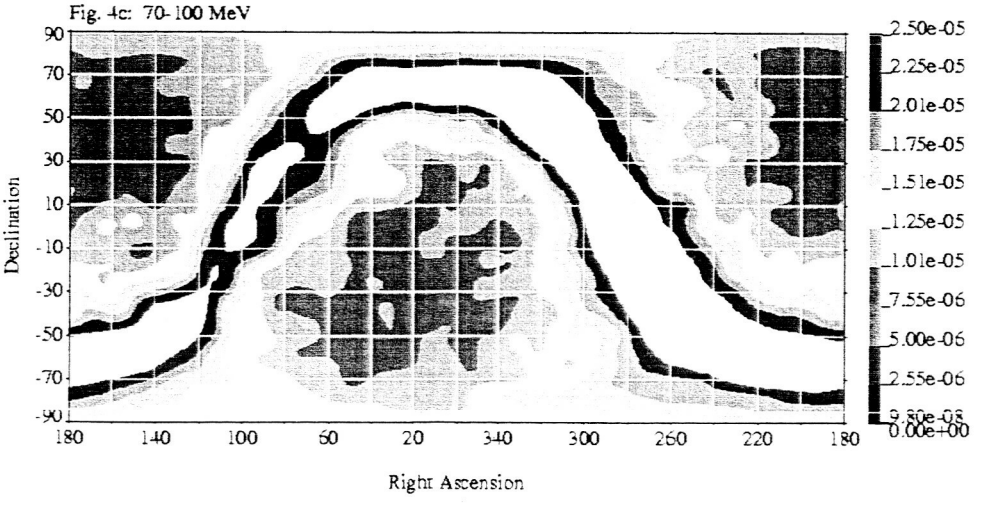

Fig. 4d: 100-150 MeV

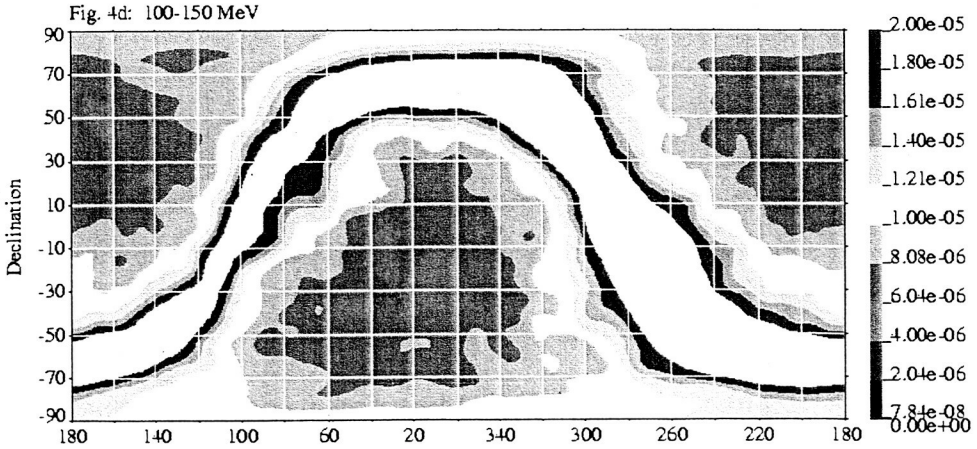

Fig. 4e: 150-300 MeV

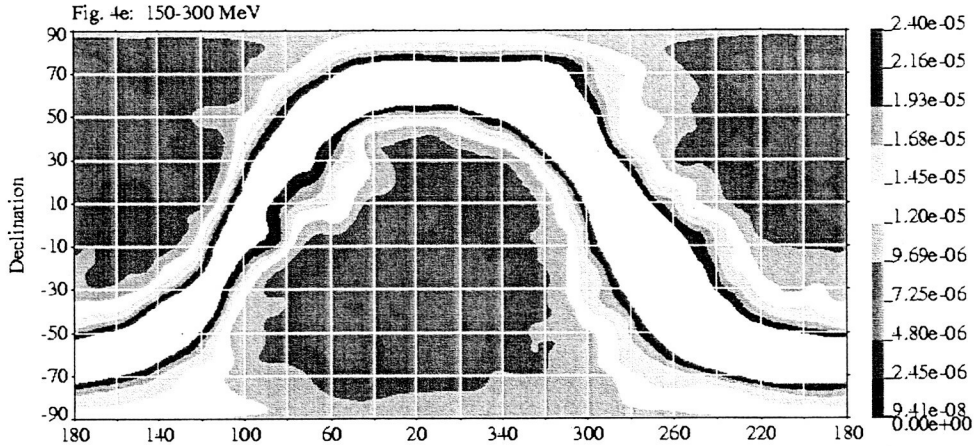

Fig. 4f: 300-500 MeV

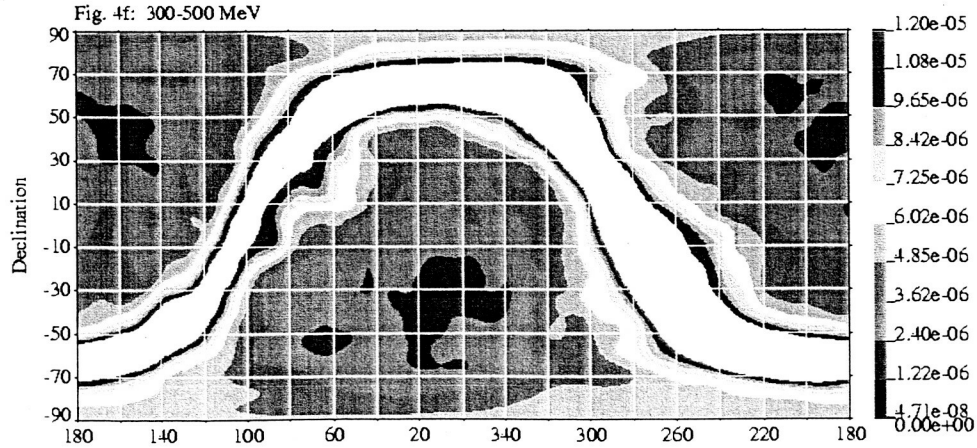

Fig. 4g: 500-1000 MeV

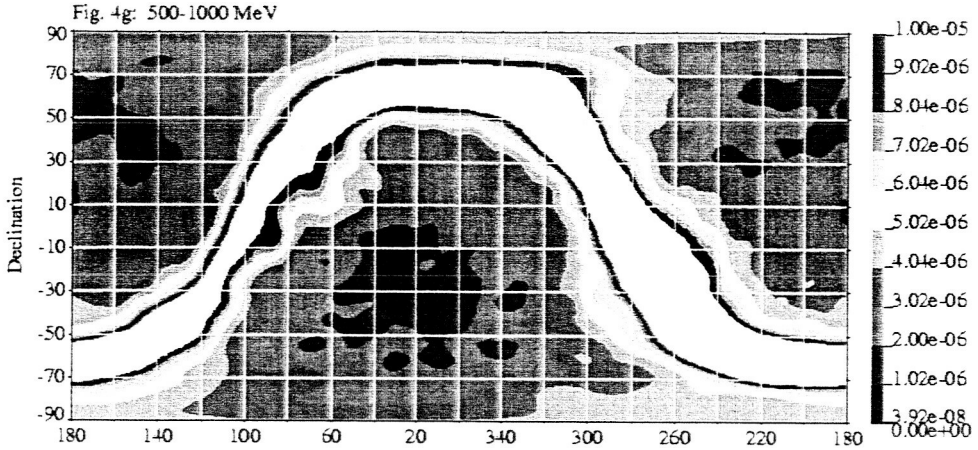

Fig. 4h: 1000-2000 MeV

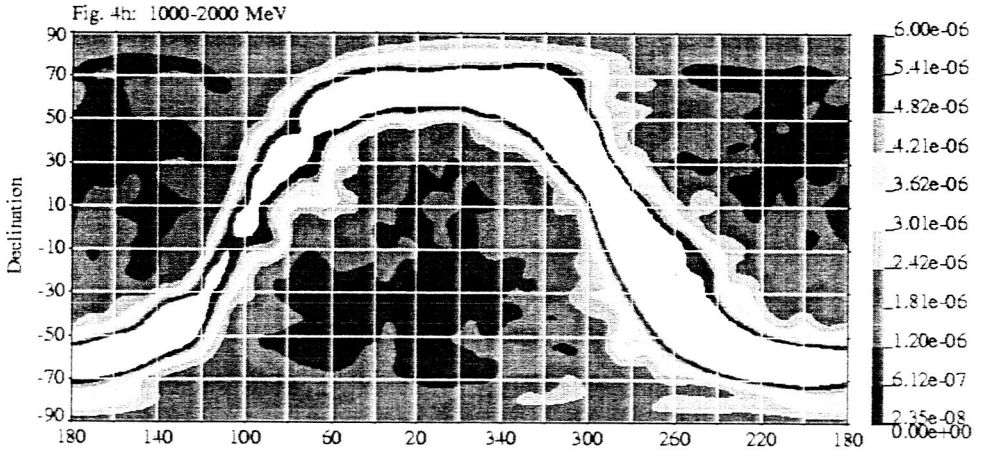

Fig. 4i: 2000-4000 MeV

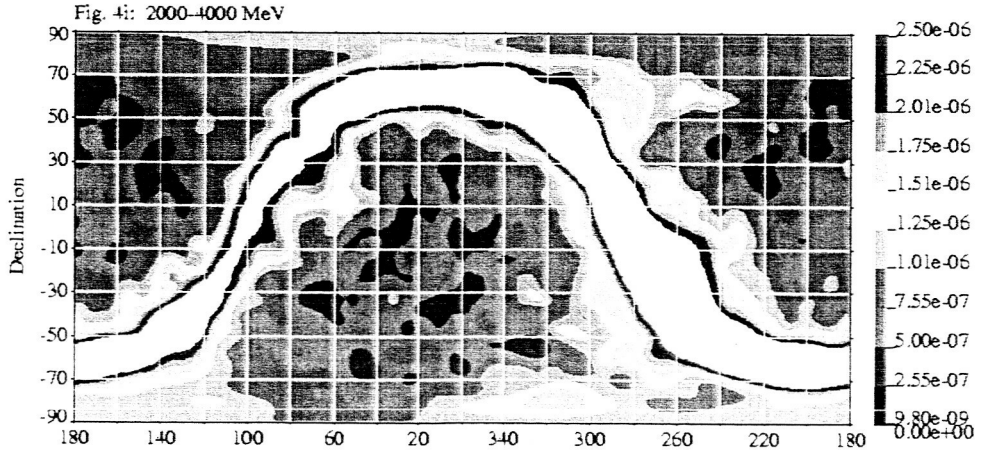

Fig. 4j: 4000-10000 MeV

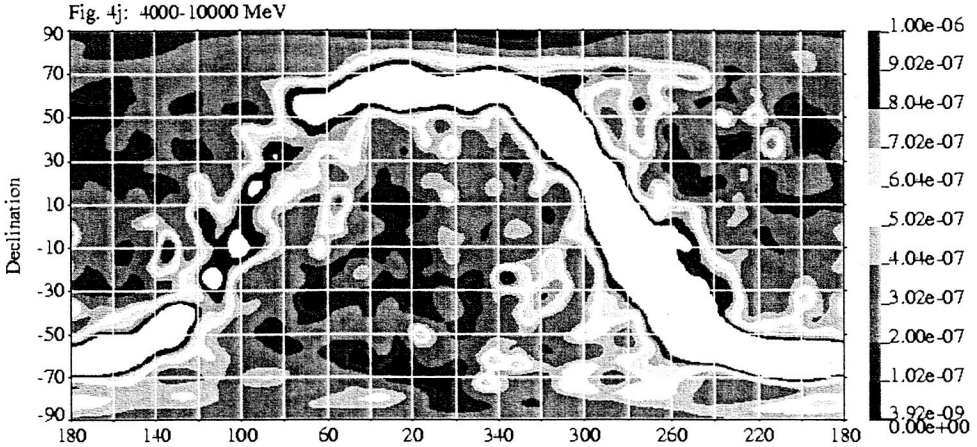

Fig. 4k: 30-100 MeV

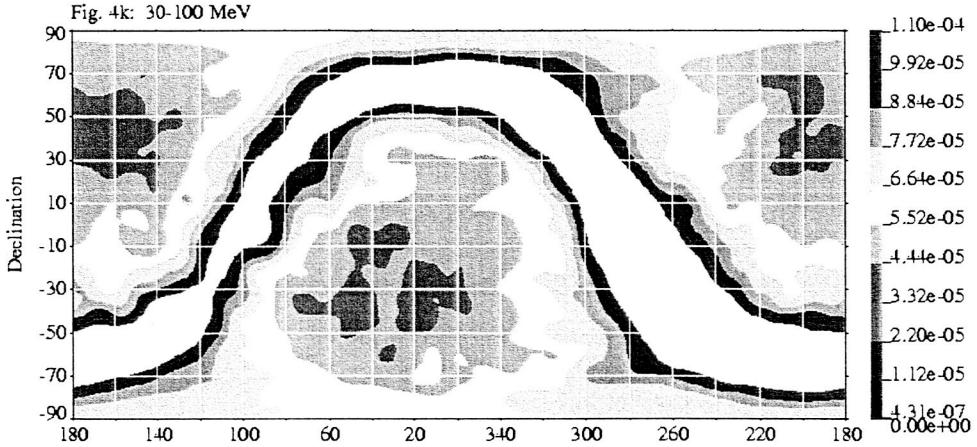

Fig. 4l: 100-300 MeV

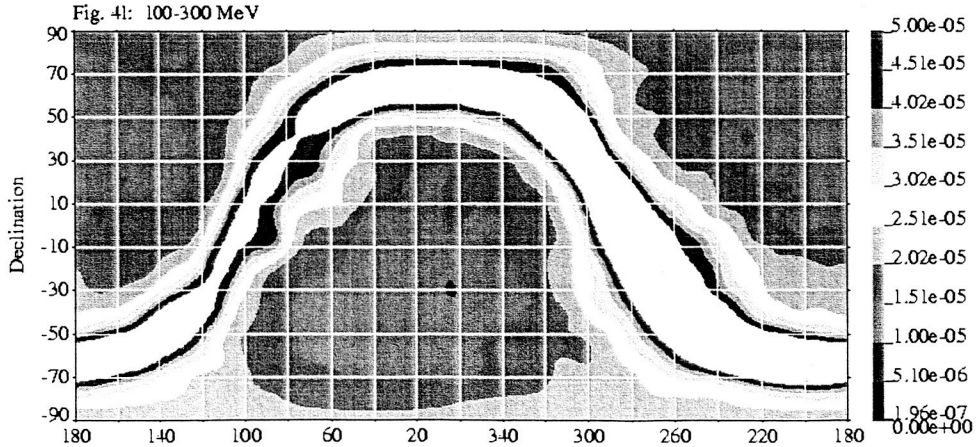

Fig. 4m: 300-1000 MeV

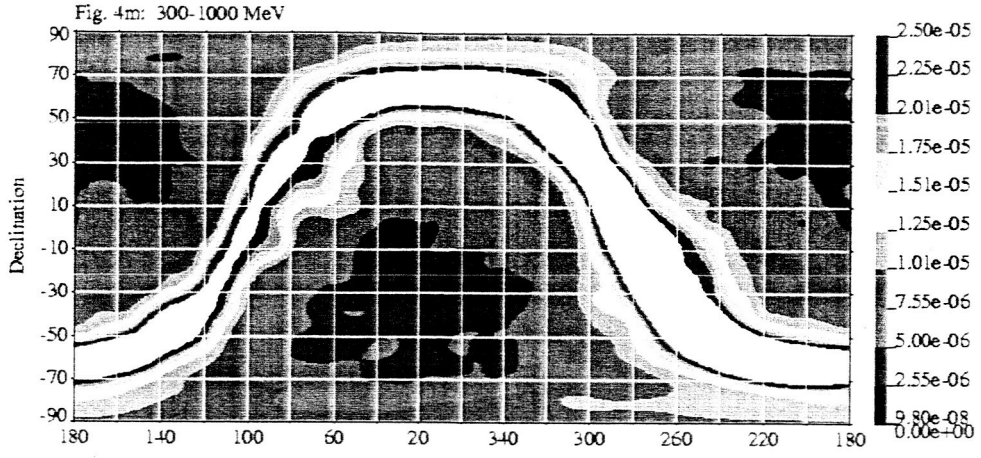

Fig. 4n: >100 MeV

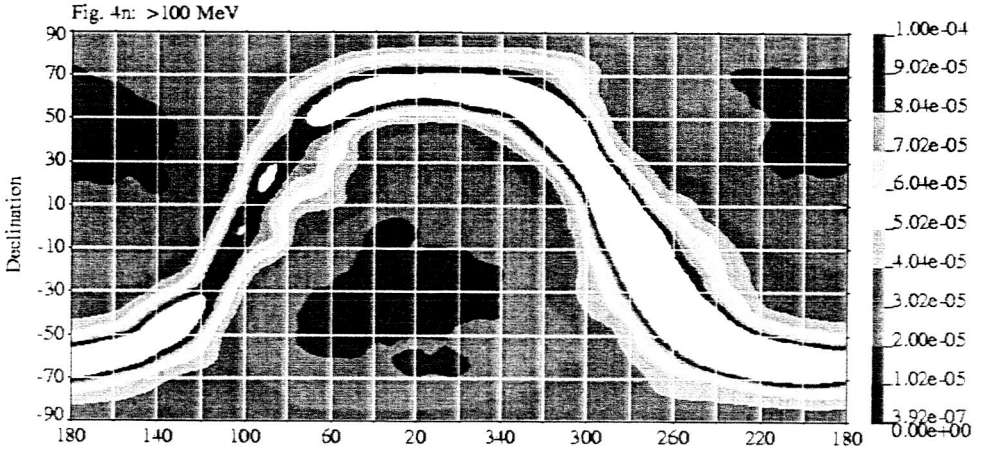

Fig. 4o: >300 MeV

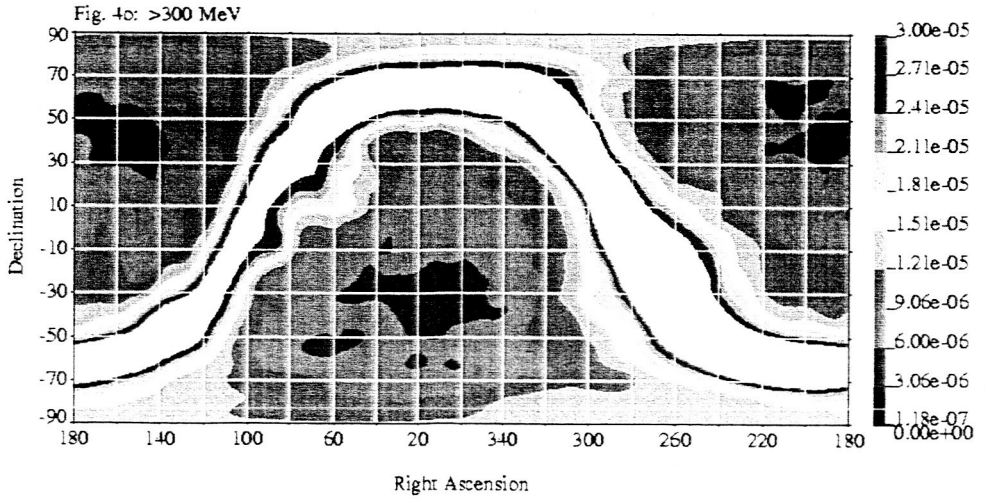

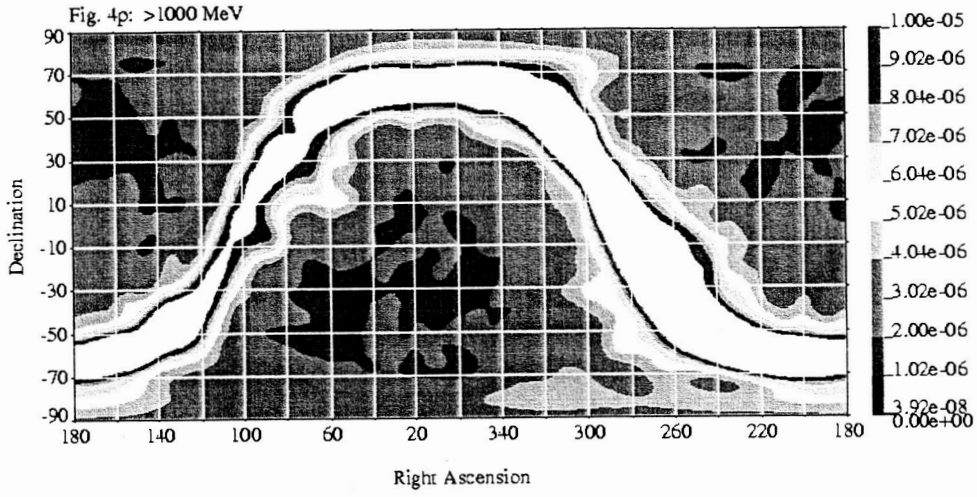

Fig. 4.— All-sky equatorial projection maps: (a) 30-50 MeV, (b) 50-70 MeV, (c) 70-100 MeV, (d) 100-150 MeV, (e) 150-300 MeV, (f) 300-500 MeV, (g) 500-1000 MeV, (h) 1000-2000 MeV, (i) 2000-4000 MeV, (j) 4000-10,000 MeV, (k) 30-100 MeV, (l) 100-300 MeV, (m) 300-1000 MeV, (n) >100 MeV, (o) >300 MeV, (p) >1000 MeV. Units of intensity are photons cm^{-2} sr^{-1} s^{-1}. Smoothing length is roughly 4°. Figures 4(a-p) are available in the electronic edition of the Journal. The printed edition contains only a sample, 4(l).

did not utilize smoothing, they used sky regions much larger than our smoothing length, thus their results were insensitive to small regions of lower intensity.

We thank D. Bertsch, S. Hunter, O. Reimer, and A. Strong for their helpful comments.

REFERENCES

Bertsch, D. L., et al. 1993, ApJ, 416, 58

Bignami, G. F., Fichtel, C. E., Kniffen, D. A., & Thompson, D. J. 1975, ApJ, 199, 54

Bignami, G. F., Fichtel, C. E., Hartman, R. C., & Thompson, D. J. 1979, ApJ, 232, 649

Esposito, J. A., et al. 1999, ApJS, 123, 203

Fichtel, C. E., Hartman, R. C., Kniffen, D. A., & Sommer, M. 1972, ApJ, 171, 31

Fichtel, C. E., et al. 1975, ApJ, 198, 163

Fichtel, C. E., et al. 1977, ApJ, 217, L9

Fichtel, C. E., Simpson, G. A., & Thompson, D. J., 1978, ApJ, 222, 833

Hartman, R. C., et al. 1979, ApJ, 230, 597

Hartman, R. C., et al. 1999, ApJS, 123, 79

Hughes, E. B., et al. 1980, IEEE NS-27, 364

Hunter, S. D., et al. 1997, ApJ, 481, 205

Kanbach, G., et al. 1988, Space Sci. Rev., 49, 69

Kanbach, G., et al. 1989, Proc. GRO Science Workshop, 2-1

Kazanas, D., & Protheroe, R. J., 1983 Nature, 302, 228

Keshet, U., Waxman, E., Loeb, A., Springel, V., & Hernquist, L. 2003, ApJ, 585, 128

Kniffen, D. A., & Fichtel, C. E. 1970, ApJ, 161, L157

Kniffen, D. A., Hartman, R. C., Thompson, D. J., & Fichtel, C. E. 1973, ApJ, 186, 105

Kraushaar, W. L., Clark, G. W., Garmire, G. P., Borken, R., Higbie, P., Leong, V., & Thorsos, T. 1972, ApJ, 177, 341

Loeb, A., & Waxman, E. 2000, Nature, 405, 156

Mayer-Hasselwander, H., et al. 1982, A&A, 105, 164

Mücke, A., & Pohl, M. 2000, MNRAS, 312, 177

Mukherjee, R., & Chiang, J. 1999, APh, 11, 213

Padovani, P., Ghisellini, G., Fabian, A. C., & Celotti, A. 1993, MNRAS, 260, L21

Page, D. N., & Hawking, S. W. 1976, ApJ, 206, 1

Pavlidou, V., & Fields, B. D. 2002, ApJ, 575, L5

Rudaz, S., & Stecker, F. W. 1991, ApJ, 368, 40

Setti, G., & Woltjer, L. 1994, ApJS, 92, 629

Silk, J., & Srednickin, M. 1984, PRL, 53, 624

Sreekumar, P., et al. 1998, ApJ, 494, 523

Stecker, F. W., & Salamon, M. H. 1996, ApJ, 464, 600

Stecker, F. 2002, hep-ph/0207323

Strong, A. W., Moskalenko, I. V., & Reimer, O. 2004, astro-ph/0405441

Strong, A. W., Moskalenko, I. V., & Reimer, O. 2004, astro-ph/0406254

Strong, A. W., Moskalenko, I. V., Reimer, O., Digel, S., & Diehl, R. 2004, astro-ph/0405275

Thompson, D. J., & Fichtel, C. E. 1982, A&A, 109, 352

Thompson, D. J., et al. 1993, ApJS, 86, 629
